

Wind-induced shear dispersion and genesis of the shelf-break front [☆]

Hsien-Wang Ou ^{*}, Dake Chen

Division of Ocean and Climate Physics, Lamont-Doherty Earth Observatory, Columbia University, 61 Route 9W, Palisades, NY 10964, United States

Received 25 October 2004; received in revised form 18 April 2005; accepted 27 March 2006

Available online 21 June 2006

Abstract

Through a simple analytical model, we examine the shear dispersion associated with oscillatory winds in an unstratified coastal ocean. As noted previously in the tidal regime, the vertical-integrated (total) horizontal diffusivity has a maximum where the water depth equals the diffusive depth – defined as the reach of the vertical diffusion during one forcing cycle. Due principally to the long synoptic timescale that characterizes the wind forcing, this depth lies over the outer shelf. When combined with effective mixing of the slope water by meso-scale eddies, the total diffusivity exhibits a minimum around the shelf break, thus facilitating frontogenesis. Due again to the long forcing period, the bottom Ekman flow is well developed at the diffusive depth, which would accentuate the gradient enhancement of the front over the inshore water, which however is bounded above by doubling.

Calculations from a primitive-equation numerical model are carried out for both unstratified and stratified oceans. From an initially uniform property gradient, a front is seen to emerge around the shelf break after an oscillating wind is switched on, in a visual demonstration of the proposed frontogenesis. The unstratified solution closely agrees with the analytical solution, and although the front is not particularly sharp, it is comparable to that observed. The stratified solution renders a more realistic simulation of the observed front, but it retains the basic features, suggesting the dominance of the proposed mechanism even in the presence of the cross-frontal circulation.

© 2006 Elsevier Ltd. All rights reserved.

1. Introduction

Off the northeastern United States, a persistent front is observed over the shelf break, the genesis of which has long intrigued oceanographers (Fedorov, 1983). In winter, the front takes on a simple form, marking a monotonic transition from the fresher shelf water to the more saline slope water (Fig. 1¹). As the shelf water

[☆] Lamont-Doherty Earth Observatory Contribution Number 6845.

^{*} Corresponding author. Tel.: +1 845 365 8338; fax: +1 845 365 8157.

E-mail address: dou@ldeo.columbia.edu (H.-W. Ou).

¹ Taken from Continental Shelf Research, vol. 8, Ou, Aikman and Houghton, “Complex empirical orthogonal function analysis of thermister chain data near a shelf-slope front”, p. 711, Fig. 1, data source originally from C. Flagg and T. Hopkins, Copyright (1988), with permission from Elsevier.

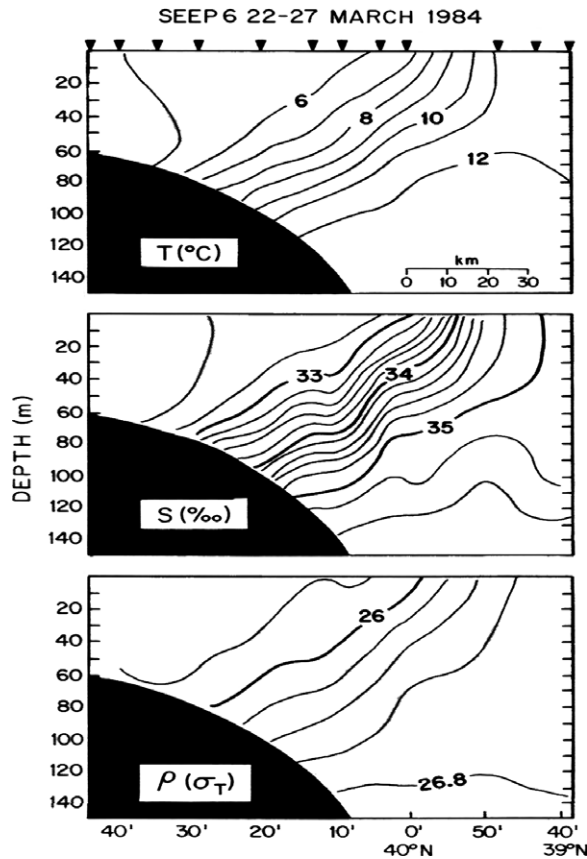


Fig. 1. A hydrographic section off the northeastern United States showing a shelf-break front in winter (taken from Ou et al., 1988, their Fig. 1, original data source from C. Flagg and T. Hopkins).

is also colder, the thermal and saline effects nearly cancel to render a weak signature in the density gradient. In summer, the radiative heating causes the seasonal thermocline to form, which dominates the density variation, but the subsurface front, being insulated from the surface heating and subjected to little horizontal mixing, retains its winter structure. As such, the summer hydrography can be described as the winter front overlaid by a seasonal thermocline, and the main challenge remains the explanation of the front in winter – the season when it must be actively formed or maintained.

Most ideas about the generation of the shelf-break front involve some form of flow convergence. For example, Chapman (1986) prescribed an alongshore flow spanning the whole shelf, so the offshore Ekman flow expels the property gradient to the shelf break where it is trapped. In Chapman and Lentz (1994) and Chapman (2000), on the other hand, the alongshore flow is not prescribed, but induced by a coastal buoyancy discharge. The same Ekman flow propels the buoyant water offshore, but only to a depth where the upstream discharge may be fully accommodated within the frontal zone (Wright, 1989) and where the Ekman flow would feed into the interfacial layer (Chapman, 2000). While this last feature is consistent with observations from tracer release experiments (Houghton, 1997; Pickart, 2000), it is a consequence – rather than the cause – of the frontal trapping given the above upstream control. In fact, it is this lack of dependence of the frontal depth on the topographic slope that led Chapman (2000) to question the relevance of the models to the genesis of the shelf-break front. To alleviate the upstream control, Narayanan and Garvine (2002) increased the horizontal diffusivity in their model, which naturally allows the buoyancy to diffuse to the shelf break, but the front also progressively weakens, unlike the observed situation.

It should be clear from above discussion that although buoyancy of the shelf water has a coastal or upstream origin, its advection by the alongshore flow does not by itself explain the frontal trapping at the shelf

break. Moreover, the observed front is well established even at the northern end of the Mid-Atlantic Bight and exhibits no systematic alongshore variation depicted in above three-dimensional models (Ullman and Cornillon, 1999). Such observations seem more supportive of the earlier view – widely shared – that the shelf-break front is fundamentally a two-dimensional phenomenon arising from cross-shore processes (e.g. Csanady, 1978; Flagg and Beardsley, 1978; Hsueh and Cushman-Roisin, 1982; Ou, 1983).

In a particularly illuminating exposition of this view, Csanady (1984) considered the frontal properties forced by the surface wind and river runoff. With the coastal buoyancy flux providing the source of the density stratification, the anchoring depth of the front – where vertical mixing just overcomes the stratification – varies in an inverse manner, which thus need not occur at the shelf break. We noted earlier that the observed shelf-break front has a rather weak density signature due to the compensating effect of temperature, one wonders therefore if a frontogenesis mechanism can be found that does not involve buoyancy forcing and which would confine the front to the shelf break.

One possible mechanism can be gleaned from the authors' explanation of the winter tidal front (Ou et al., 2003). In the tidal regime, it is well recognized the importance of shear dispersion in the horizontal mixing (Fisher et al., 1979; Zimmerman, 1986; Geyer and Signell, 1992) and the resulting diffusivity has strong depth dependence, dropping sharply around the tidal friction depth (Okubo, 1967). When combined with small background diffusivity, Ou et al. (2003) found that the vertical-integrated diffusivity exhibits a minimum in the mid-shelf, which may possibly account for the tidal front observed in the unstratified winter season (Hill and Simpson, 1989; Ullman and Cornillon, 1999). Farther offshore, with rapidly diminishing tidal currents, the shear dispersion would be dominated by wind-induced motion; but surprisingly, despite its potential importance to the horizontal mixing and hence property distribution, the process has not been examined to any significant degree in the literature. Some obvious questions include: What is the mechanics of wind-induced shear dispersion? What is the magnitude of the effective diffusivity and how does it vary across the shelf? And, particularly, can it lead to the generation of the shelf-break front? It is the desire to address these questions that motivates the present study.

For the organization of the paper, we first consider in Section 2 an analytical model to elucidate the physics of wind-induced shear dispersion, and show that it may lead to frontogenesis around the shelf break. In Section 3, numerical calculations are carried out to validate and extend the analytical results, and to compare the model front with observations. The paper is concluded by a discussion in Section 4.

2. Analytical model

To elucidate the essential physics, we consider an ocean homogeneous in density and forced by uniform along-shore wind oscillating at period T . The model domain, as sketched in Fig. 2, comprises of a cross-shore section of the shelf-slope that is unvarying in the along-shore direction. A right-handed Cartesian coordinate system is used with x - and z -axis directed offshore and up, respectively.

2.1. Wind-driven motion

Unlike tidal currents, which may be assigned a linear profile in the vertical (Okubo, 1967), the wind-induced shear is concentrated in Ekman layers, so a dynamical model, however rudimentary, needs to be first constructed for the wind-driven motion. We consider the momentum equations of the form (e.g. Csanady, 1982)

$$u_t - f\bar{v} = -g\eta_x + \nu u_{zz}, \quad (2.1)$$

$$v_t + fu = \nu v_{zz}, \quad (2.2)$$

where all symbols are conventional, with f being the Coriolis parameter, g , the gravitational acceleration, ν , the vertical viscosity (taken to be the same as the vertical diffusivity), and partial derivatives are indicated by subscripts. Since we are outside the surf zone, we assume the vertical diffusivity to be linked to the wind-stress amplitude $|\tau|$ via

$$\nu = \frac{|\tau|/\rho_0}{100\pi f}, \quad (2.3)$$

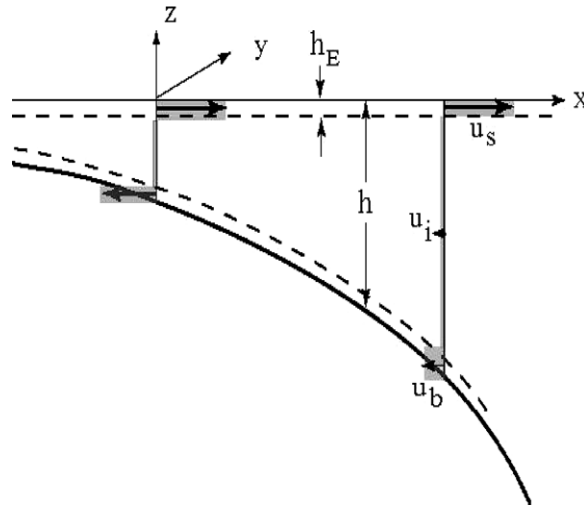


Fig. 2. A schematic of the wind-driven model in which the cross-shore flow is divided into slabs of Ekman layers and the interior. Also indicated are the slab motions at the peak of the positive wind, corresponding to the analytical solution shown in Fig. 3 (the standard case).

based on Csanady (1982, his Eq. 6.22b, but averaged over the forcing cycle), with ρ_0 being the ocean density, assumed constant. The boundary conditions at the surface and bottom are:

$$v(u_z, v_z) = (0, \tau/\rho_0) \quad \text{at } z = 0 \tag{2.4}$$

and

$$v(u_z, v_z) = \alpha^*(u, v) \quad \text{at } z = -h, \tag{2.5}$$

where α^* is the resistance coefficient, assumed constant for simplicity (see Csanady, 1982). Since the shelf width is small compared with the barotropic deformation radius, the surface may be taken to be rigid, so the continuity equation yields

$$\int_{-h}^0 u \, dz = 0 \tag{2.6}$$

in the presence of a coastal boundary. As formulated, the water depth enters the problem only parametrically; the problem thus remains effectively one-dimensional with z constituting the only independent variable. The flow is of the Ekman type, but extended here to include time-dependence and coastal constraint – all are required elements for a minimal model.

If one decomposes the velocity into its vertical average (overhat) and deviation (primed) – referred, respectively, as the barotropic and baroclinic components,

$$u = \hat{u} + u', \text{ etc.}, \tag{2.7}$$

the barotropic flow then satisfies the equations

$$\hat{u} = 0, \tag{2.8}$$

$$\hat{v}_t = \frac{1}{h} \left(\frac{\tau}{\rho_0} - \alpha^* \hat{v} \right). \tag{2.9}$$

In anticipating later discussion, we define as diffusive depth the reach of vertical diffusion during one forcing cycle,

$$h_d = (vT)^{1/2}, \tag{2.10}$$

and non-dimensionalize the variables by the scales (square brackets) that $[t] = T$, $[h] = h_d$, and $[\hat{v}] = |\tau|T/\rho_0 h_d$. Defining a dimensionless resistance coefficient

$$\alpha \equiv \alpha^* T / h_d, \tag{2.11}$$

then, apart from the oscillatory factor $\exp(-i2\pi t)$, (2.9) can be solved to yield, in dimensionless form,

$$\hat{v} = (\alpha - i2\pi h)^{-1}. \tag{2.12}$$

As expected, if friction dominates, as is the case of large resistance coefficient, long forcing period or shallow depth, the barotropic along-shore flow varies in phase with the wind; but in the inviscid limit, it lags the wind by a quarter cycle.

For the baroclinic flow, it is non-dimensionalized by $[u', v'] = |\tau|(\rho_0 f h_E)^{-1}$, with $h_E \equiv (2\nu/f)^{1/2}$ being the Ekman depth. Since most wind energy is in the synoptic band, we assume

$$T \gg f^{-1}, \tag{2.13}$$

so the (non-dimensionalized) baroclinic flow is governed by the equations:

$$-v' = \frac{1}{2} E u'_{zz}, \tag{2.14}$$

$$u' = \frac{1}{2} E v'_{zz} + i2\pi E^{1/2} \hat{v}, \tag{2.15}$$

where $E \equiv (h_E/h_d)^2 = 2(fT)^{-1}$ is the Ekman number, small on account of (2.13). With the non-dimensionalization, the boundary conditions (2.4) and (2.5) become

$$(u'_z, v'_z) = (0, 2E^{-1/2}) \quad \text{at } z = 0 \tag{2.16}$$

and

$$(u'_z, v'_z) = (0, 2E^{-1/2} \alpha \hat{v}) \quad \text{at } z = -h. \tag{2.17}$$

The solution is of the Ekman type, modified by time-dependence. While this solution is simple enough, it would drive a more complicated property perturbation when subjected to vertical diffusion; and this in turn would lead to rather unwieldy algebra when one attempts to derive the property flux as the latter involves product of the two dependent variables, followed by vertical integration. Some mathematical simplification is thus called for.

For this purpose, one notes from the Ekman solution that vertical shear in the cross-shore current – the only relevant component here – is concentrated at the outer boundary of the Ekman layer. One thus may preserve the shear advection by approximating the flow as moving slabs of surface and bottom Ekman layers and the interior (denoted, respectively, by subscripts s, b, and i). Obviously there is an interior only if the water depth is greater than twice the Ekman depth, to which we limit our analytical solution. With the slab approximation, (2.15) can be integrated vertically to yield

$$\begin{aligned} u'_s &= 1 + i2\pi\lambda\hat{v} & \text{for } 0 > z > -\lambda, \\ u'_i &= i2\pi\lambda\hat{v} & \text{for } -\lambda > z > -h + \lambda, \\ u'_b &= -1 - i2\pi(h - \lambda)\hat{v} & \text{for } -h + \lambda > z > -h, \end{aligned} \tag{2.18}$$

where $\lambda \equiv E^{1/2}$ is the scaled Ekman-layer depth. As a representative example, we have plotted in Fig. 3 the solution (2.12) and (2.18) for the case of $\lambda = 0.15$ and $\alpha = 10$ (noting that the alongshore flow is scaled differently from the cross-shore flows).

As alluded earlier, the alongshore flow is in phase with the wind in the shallow water, but lags by a quarter cycle in the deep water where the bottom friction is negligible. Concurrently, there are equal and opposite Ekman flows in the shallow water, but only surface Ekman flow in the deep ocean. Since the time-change term is small in the Ekman layers, the surface flow is in phase with wind, while the bottom flow out of phase with the alongshore flow. The interior flow on the other hand mimics in amplitude the alongshore flow, but lags it by a quarter cycle due to the inviscid balance. With the above, the wind-driven motion shown in Fig. 3 is largely explained. To aid the visualization, the cross-shore flow at the peak of the positive wind is also shown in Fig. 2. The presence of finite surface flow in the far field constitutes a major difference from the tidal flow, which has significant implications on the horizontal diffusivity, as seen later (Section 2.3).

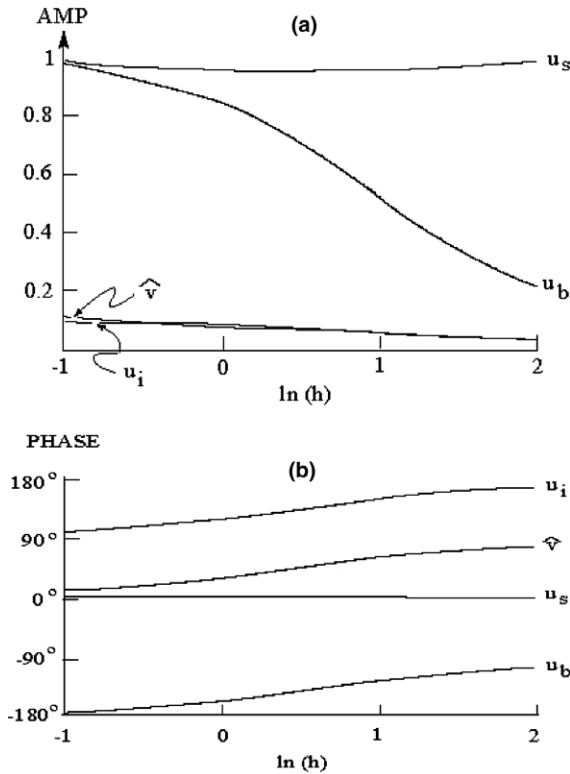


Fig. 3. (a) The amplitude of the wind-driven motion, plotted against bottom depth; (b) same as (a) but for the phase.

2.2. Tracer concentration

We next consider the concentration of a passive tracer governed by the equation

$$C_t + (uC)_x + (wC)_z = \nu C_{zz}. \tag{2.19}$$

As the concentration is used later to represent salinity – which best defines the shelf-break front, it is assumed to satisfy the zero normal flux condition at the top and bottom surfaces, or approximately,

$$C_z = 0 \quad \text{at } z = 0, -h \tag{2.20}$$

and is subjected to a cross-shore flux F at the coast, signifying the freshwater source. Since we are concerned with the time-mean field as to whether it exhibits frontal structure, we decompose C into its time-mean over T (overbarred) and deviation from this mean (primed)

$$C = \bar{C} + C'. \tag{2.21}$$

For simplicity, we neglect the vertical variation of the mean field (see discussion in Section 3.2), so the equation governing the time-mean may be integrated vertically to yield

$$h\bar{C}_t + \left(\int_{-h}^0 \overline{u'C'} dz \right)_x = 0, \tag{2.22}$$

where u' can be equated with the baroclinic motion derived earlier since, in an unstratified ocean, the time-mean cross-shore flow has no vertical structure, so (2.8) implies that both time-mean and fluctuating components of the barotropic cross-shore flow vanish. Eq. (2.22) states that there could be secular change in the mean concentration if the wind-induced flux has divergence.

The perturbation concentration, on the other hand, satisfies the equation

$$C'_t + u'\overline{C}_x = vC'_{zz}, \tag{2.23}$$

in which we have neglected higher-harmonic terms. It is seen that the perturbation field is induced by wind-driven motion and modified by vertical diffusion – the latter being what causes the phase shift to facilitate a finite flux. Moreover, it is noted that the perturbation is coupled to the mean property gradient, still unknown but the main property of interest. This coupling however may be filtered out by defining a horizontal diffusivity κ via

$$u'C' = -\kappa\overline{C}_x. \tag{2.24}$$

Given the wind-driven motion u' (2.18), one may solve C' from (2.23), which is linear in the unknown \overline{C}_x . This solution can be substituted into (2.24) to yield a diffusivity that is a function *only* of the motion field since \overline{C}_x would cancel out from both sides.

Substituting (2.24) into (2.22), the mean field evolves according to

$$h\overline{C}_t - (k\overline{C}_x)_x = 0, \tag{2.25}$$

where

$$k \equiv \int_{-h}^0 \kappa dz \tag{2.26}$$

is referred as the “total” diffusivity, again a function only of the motion field. With the total diffusivity known, one may use (2.25) to examine the evolution of the mean field given its initial distribution. In the steady state, (2.25) can be integrated cross-shore to yield

$$F = -k\overline{C}_x, \tag{2.27}$$

that is, the cross-shore flux must now be uniform across the model domain and hence assumes its coastal value F , an external parameter. With (2.27), the mean property gradient is fully determined, and since it is inversely proportional to the total diffusivity, it has a maximum where the total diffusivity is minimum, signifying frontogenesis. The remaining task is simply to calculate the total diffusivity to see if it indeed exhibits a minimum near the shelf break.

2.3. Horizontal diffusivity

Since the basic physics is similar to that of the tidal dispersion, we scale the horizontal diffusivity as $[\kappa] = [u']^2[h]^2(240v)^{-1} = 0.42T|\tau|/\rho_0$, which thus increases linearly with the forcing amplitude and period. Adopting additionally that $[C'] = F([h][u'])^{-1}$ and $[\overline{C}_x] = F([h][\kappa])^{-1}$, (2.23) is non-dimensionalized to

$$C'_{zz} + i2\pi C' = au', \tag{2.28}$$

where $a \equiv 240\overline{C}_x$. Analytical expression for the tracer concentration is presented in the Appendix and, apart from the unknown multiplication factor a , plotted in Fig. 4a and b for the case of $\lambda = 0.15$ and $\alpha = 10$. Notice that the vertical coordinate has been scaled by the local water depth, with the dashed and dotted lines marking the boundaries of the Ekman layers and the diffusive depth, respectively. Since the tracer signal is generated by advection, it is greatest in the Ekman layers, which however is short-circuited in the shallow water by vertical mixing and vanishes in the bottom Ekman layer in the far field, as expected from the cross-shore flow shown in Fig. 3a. Since the balance in the Ekman layers is dominated by diffusion and advection, the signal there is approximately out of phase with the Ekman flows (since the mean property gradient is positive), and phase propagation is more prevalent outside the Ekman layers but within the diffusive depth. With the above, the tracer perturbation shown is largely explained.

With the perturbation field known, one may calculate the property flux and the horizontal diffusivity via (2.24), the latter being plotted in Fig. 4c. As expected, this diffusivity is highly heterogeneous in the vertical, being mostly confined to the Ekman layers of significant cross-shore flow. In Fig. 5, we have plotted the vertically averaged (thin solid) and integrated (thick solid) horizontal diffusivities, which exhibit

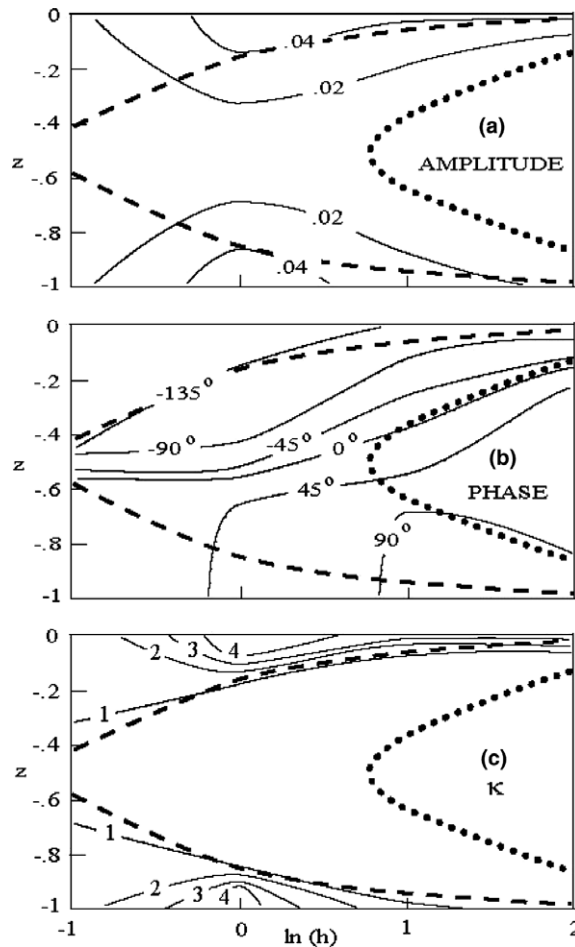


Fig. 4. (a) The amplitude of the property perturbation, plotted as contours on a cross-shore section. The vertical coordinate has been normalized by the local water depth, and the dashed and dotted lines mark the boundaries of the Ekman layers and diffusive depths, respectively; (b) same as (a) but for the phase; (c) same as (a), but for the wind-induced horizontal diffusivity.

both similarities and differences when compared with the tidal diffusivity (Ou et al., 2003). As in the tidal case, the vertically averaged diffusivity levels off in the shallow water since the expanding coverage by the Ekman layer (relative to the water column) is countered by enhanced vertical mixing. As such, the total diffusivity peaks at the diffusive depth where the tracer perturbation caused by differential advection would mix through the water column during one forcing cycle – thus making for the most efficient shear dispersion. But in contrast to the tidal case, the total diffusivity, instead of going to zero, approaches a finite constant in the far field associated with undiminished surface Ekman flow. The enhancement of the maximum over the far-field value thus is due solely to the additional shear dispersion associated with the bottom Ekman flow; it depends therefore on the importance of bottom friction at the diffusive depth and in any event it is less than doubling.

We have so far considered the wind-induced shear dispersion, which yields a total diffusivity that peaks at diffusive depth and approaches a finite constant in the far field. Additional physics obviously is needed to produce an offshore minimum to facilitate frontogenesis – the same requirement as in the tidal case (Ou et al., 2003). In that case, we have assumed constant non-tidal background diffusivity (hence increases linearly with depth when vertically integrated) without being specific about its source. The present derivation shows that this background diffusivity can be provided by wind-induced shear dispersion; and in fact the inshore decrease in the total diffusivity shown in Fig. 5 is precisely that assumed by Ou et al. (2003) to limit the offshore boundary of the tidal front.

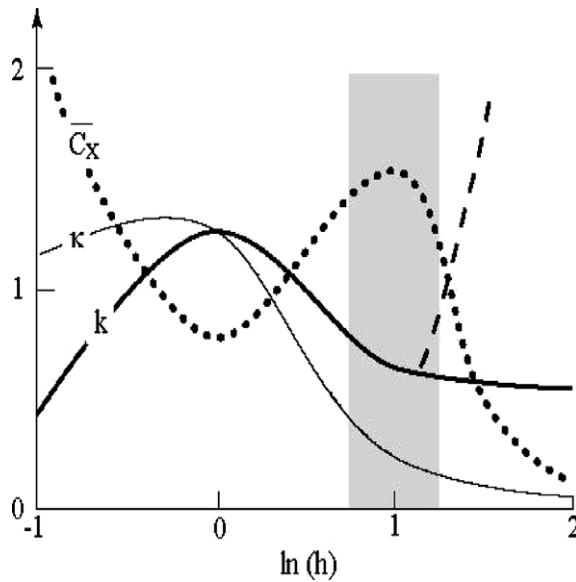


Fig. 5. The vertically averaged (thin solid) and integrated (thick solid) diffusivity due to wind-induced shear dispersion, and the modification of the latter by the eddy-induced mixing (thick dashed), plotted against the bottom depth. Also plotted in the dotted line is the cross-shore gradient of the mean property concentration, which shows a maximum over the shelf break, as indicated by the shaded column.

In the present case, with the wind extending the horizontal mixing beyond the depths of the tidal regime, a plausible mechanism for the offshore, non-wind mixing is the meso-scale eddies, which are prevalent in the slope waters (Churchill et al., 1993; Gawarkiewicz et al., 2001), but – because of their large vertical extent – are impeded from penetrating onto the shelf by the vorticity constraint. Obviously one may not assign a definitive diffusivity to such irregular mixing events, but to incorporate the above topographic constraint on the eddy motion, we shall simply set a horizontal diffusivity that increases linearly with depth from a zero value at some upper slope depth to an asymptotic deep-ocean value. When integrated vertically, the total diffusivity thus increases even more rapidly with depth (quadratic in this case), which would modify the total diffusivity as indicated in the dashed line in Fig. 5.

With the combination of the wind- and eddy-induced horizontal mixing, the total diffusivity thus has a minimum (the shaded column in Fig. 5) where the eddy diffusivity sets in so long as this depth is greater than the diffusive depth, assumed to be the case. According to (2.27), this minimum in total diffusivity would be accompanied by maximum in the property gradient (the dotted line): we have thus identified a mechanism of frontogenesis at the shelf break stemming from enhanced horizontal mixing to either side. One sees that although the above specification of the eddy-induced diffusivity is somewhat arbitrary, the only requirement for the proposed frontogenesis is that this diffusivity does not become appreciable until beyond the diffusive depth, a condition as seen later to be generally met.

2.4. Application

The basic physics of the proposed frontogenesis thus is rather simple: it is the mixing from both sides – wind from the inshore and eddies from the offshore – that confines the property gradient. Whether the model may explain the observed front at the shelf break requires more detailed assessments, which will proceed in two steps: we first use representative parameter values (referred as the standard case) to see if the model may reproduce the observed front; we then examine the parameter dependence of the model front to see how robust or sensitive it is.

Based on the wind spectrum in winter (for example, Beardsley et al., 1985), we take as standard forcing a wind-stress amplitude of 1.5 dyne cm^{-2} oscillating at 10-day period. Setting $f = 10^{-4} \text{ s}^{-1}$ for mid-latitudes and

a resistance coefficient of $\alpha^* = 0.75 \times 10^{-3} \text{ m s}^{-1}$ (attained by drag coefficient of $C_D = 3 \times 10^{-3}$ and turbulent velocity of 25 cm s^{-1}), we estimate a vertical diffusivity of $50 \text{ cm}^2 \text{ s}^{-1}$, an Ekman depth of 10 m, an Ekman flow of 15 cm s^{-1} , a diffusive depth of 66 m, and the scale of the horizontal diffusivity of $54 \text{ m}^2 \text{ s}^{-1}$. The scaled Ekman depth is then $\lambda = 0.15$ and the non-dimensionalized resistance coefficient $\alpha = 10$, incidentally the values used in Figs. 2–5. For the eddy-induced horizontal diffusivity shown in Fig. 5, it is zero at 200 m and increases linearly with depth to a value of $100 \text{ m}^2 \text{ s}^{-1}$ at 1000 m.

It is seen therefore that principally due to the long forcing period, the associated diffusive depth lies over the outer shelf, which nonetheless is sufficiently separated from the onset of the eddy mixing to facilitate a shelf-break front. Due again to the long forcing period, the bottom Ekman flow is well developed over the shelf, so the gradient enhancement of the front over the shelf water is close to the maximum allowed – that is, doubling. Although this gradient contrast is not remarkable, it is seen later (Section 3.2) to be commensurate with that observed.

With this favorable observational comparison of the standard solution, we shall next examine the sensitivity of the model solution to changing external parameters. Although the prescribed eddy-induced diffusivity is somewhat arbitrary, this uncertainty is mollified to some degree by the steep topography over the slope, which sharply curbs the offshore boundary of the front. As such, the frontal properties are primarily functions of the wind-stress forcing: its amplitude and period. In particular, we discern the following functional dependence based on scale definitions: the diffusive depth $h_d \propto |\tau|^{1/2} T^{1/2}$, the scaled Ekman depth $\lambda \propto T^{-1/2}$, the non-dimensionalized resistance coefficient $\alpha \propto |\tau|^{-1/2} T^{1/2}$. The last dependence on the forcing amplitude is likely over-estimated since the (dimensional) resistance coefficient should increase with wind strength, rather than being a constant, as assumed. One notes that all these dependences are half-power, hence weaker than the linear dependence. Also relevant to the later discussion, we note that the scale of the horizontal diffusivity varies as $[\kappa] \propto T|\tau|$, so the total diffusivity varies as $[h][\kappa] \propto T^{3/2}|\tau|^{3/2}$.

We first consider the effect of changing forcing amplitude. A stronger wind would increase the diffusive depth – the depth scale of Fig. 5, thus expelling the property gradient to greater depth. But even with the standard wind, which is on the lower end of its observed strength, the front is already located at the shelf break, so one expects the topographic anchoring of the front to be a rather robust feature with regard to this change. Changing the wind amplitude also alters the value of the dimensionless resistance coefficient (see the preceding paragraph) and hence possibly the diffusivity pattern. To see this, we have plotted in Fig. 6 the wind-induced total diffusivity for different values of the dimensionless parameters. The thick solid line is for the standard solution, and the two curves immediately above and below are for the cases when the wind amplitude is halved and doubled, respectively. A stronger wind, for example, would decrease α and, with it, the maximum diffu-

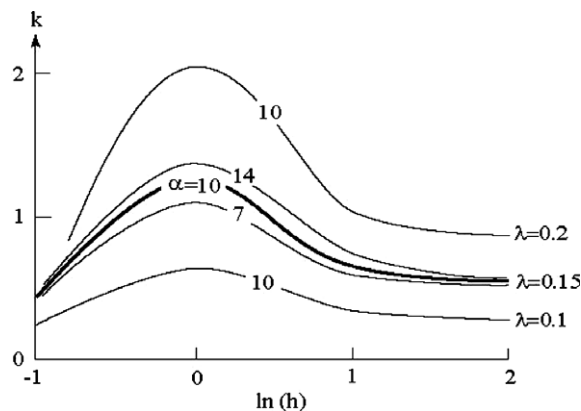


Fig. 6. Total diffusivity plotted as a function of the bottom depth for different values of the scaled Ekman depth λ and the non-dimensionalized resistance coefficient α . The thick solid line represents the standard case, and the different dimensionless values correspond to changes in forcing amplitude and period – by halving and doubling. The thin lines immediately above and below the standard curve have their forcing amplitude halved and doubled, respectively. Farther outward of the envelope, the upper and lower curves have their forcing period halved and doubled (the forcing amplitude is correspondingly halved and doubled to maintain the same α).

sivity and – hence – the gradient contrast of the front. But since α remains large even for the doubling of the wind amplitude, the gradient contrast is not significantly weakened. Dimensionally, the total diffusivity increases with the wind amplitude (seen above to vary in the three-half power), which however does not impact on the relative gradient contrast.

We next consider the effect of increasing forcing period. Just like the stronger wind, it would expel the diffusive depth offshore to narrow the frontal zone. It also decreases λ to affect the total diffusivity. To see this, we have plotted in Fig. 6 additional curves straddling the standard solution with the λ values corresponding to halving and doubling of the forcing period (but keeping the same α value, meaning that the forcing amplitude is correspondingly adjusted). The dependence of the total diffusivity on the forcing period is T^{-1} since the scaled Ekman layer thins as $T^{-1/2}$, which leads to a reduction of perturbation signal as $T^{-1/2}$ and – hence – a vertical integrated flux as T^{-1} . But since the scale of the total diffusivity is seen above to vary as $T^{3/2}$, the total diffusivity at the diffusive depth actually increases as $T^{1/2}$ in dimensional unit. In other words, the longer period wind would have greater effect on the frontal properties, which partly justifies the relatively long forcing period used in the standard case. Increasing forcing period also augments α , which would further enhance the gradient contrast to its upper bound. As hinted earlier, however, if the forcing period were so long that the wind and eddy mixing overlap significantly, the frontal gradient would be weakened.

To recap, the parameter dependence of the frontal properties accentuates the effect of the longer period wind even though the wind spectrum is relatively flat in the synoptic band. As a consequence, the front tends to be strongly confined to the shelf break – being expelled there from the inshore side by the synoptic wind and curbed on the offshore side by the mixing associated with meso-scale eddies. Moreover, the synoptic wind also assures a maximum gradient contrast between the front and the inshore water, which, though not particularly sharp, is nonetheless commensurate with that observed.

3. Numerical study

3.1. The model

We have carried out a numerical study of the problem using a primitive-equation coastal-ocean model (Wang, 1982), which has been previously applied to various coastal studies, including fronts (Chen et al., 2003a,b). The model uses Mellor's (1982) level-2.5 turbulence closure scheme for the vertical mixing and Smolarkiewicz's (1984) anti-diffusive scheme for the tracer advection – both essential in minimizing non-physical mixing and maintaining the frontal sharpness. The background horizontal diffusivity is set to a small value of $1 \text{ m}^2 \text{ s}^{-1}$ so as not to interfere with the dynamical diffusivity due to wind-induced shear dispersion or the eddy-induced diffusivity, the latter being prescribed as in the analytical model (see Section 2.4).

For the present application, the model is configured on a two-dimensional cross-shore section with exponential topography (see Fig. 7, noting however that, for display purpose, the vertical column shallower than 100 m has been stretched twofold). The horizontal resolution is 500 m, and the vertical grid spacing is 5 m in the top 100 m and 10 m in the rest of the water column. The model domain has a width of 100 km and a depth varying from 20 m at the coast to 500 m offshore. The cross-shore flow is set to zero at the coast and subjected to radiation condition at the offshore boundary. To ensure equilibrium state, salinity and temperature are specified at both inshore and offshore boundaries with $(S, T) = (32.3^0/00, 3 \text{ }^\circ\text{C})$ and $(35.3^0/00, 13 \text{ }^\circ\text{C})$, respectively. The only external forcing is a periodic along-shore wind-stress.

Based on observations, we take the inshore water as being fresher and colder – but only slightly lighter – than the offshore water. Initially, both salinity and temperature have uniform cross-shore gradient, and we want to see if the gradient sharpens near the shelf break after the wind forcing is switched on. Since the model has no heat or salt fluxes at the surface, the salinity and temperature distribution – when normalized by their cross-shore range – are identical, it suffices therefore to describe only the salinity field, whose initial distribution is shown in Fig. 7a. Two sets of experiments are carried out, with the equation of state switched off and on, referred below as unstratified and stratified cases, respectively. The unstratified run allows a closer comparison with the analytical model, and the stratified run provides a more realistic simulation of the observed situation. For a closer comparison with the analytical solution, the vertical diffusivity in the unstratified run, rather than its nominal parameterization, is set to a constant in accordance with (2.3).

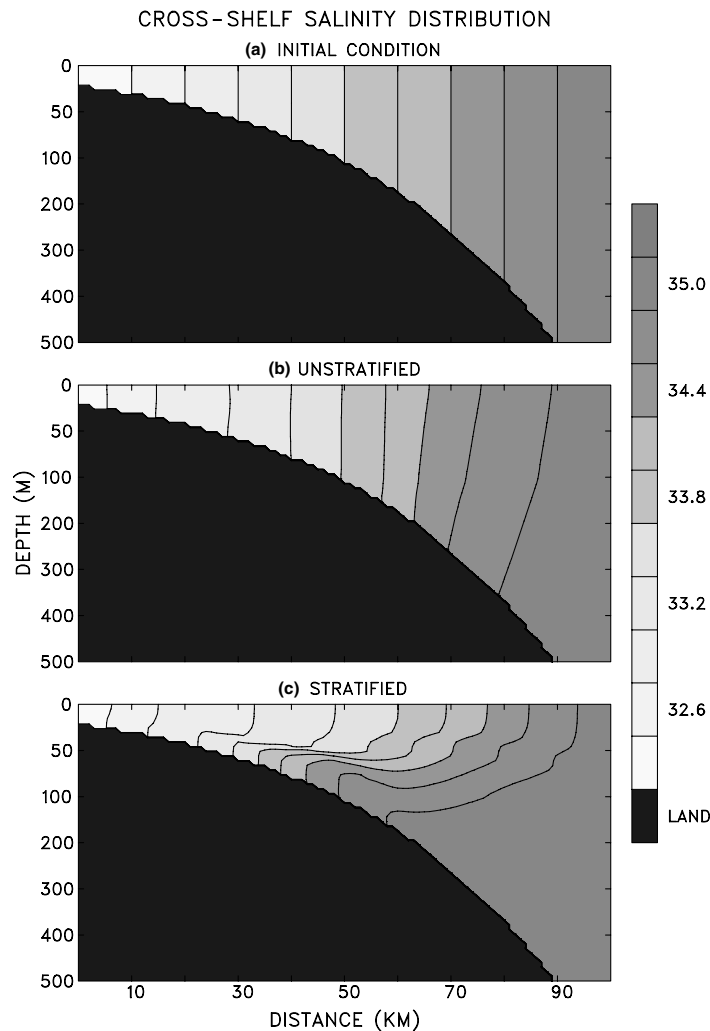


Fig. 7. (a) The initial salinity field of uniform horizontal gradient; (b) the salinity field averaged over an equilibrium cycle for the unstratified case, which shows the frontogenesis at the shelf break; (c) same as (b) but for the stratified case. Note that the vertical column shallower than 100 m has been stretched twofold for display purpose.

3.2. Unstratified solution

With the equation of state turned off, the density remains homogeneous through the numerical integration. As such, the salinity is passive, just as the property field considered in the analytical model. We use the same forcing as the standard analytical case, so the wind-stress has an amplitude of 1.5 dyne cm^{-2} and a period of 10 days. A cursory examination of the numerical solution shows that it has reached quasi-equilibrium after about 50 cycles, and only the equilibrium solution is shown in the following discussion. As a check of the wind-driven model, the cross-shore flow at the peak of the positive wind (not shown) closely resembles that of Fig. 2. In particular, it supports the slab approximation and shows a well-developed bottom Ekman flow on the shelf, which vanishes in the far field.

The salinity averaged over the fiftieth cycle is plotted in Fig. 7b, which shows a distinct sharpening of the gradient at the shelf break at the expense of the surrounding water. Given the absence of density stratification and hence buoyancy-driven circulation, the most likely source for the gradient change is the shear dispersion; the numerical solution thus provides a palpable visual demonstration of the proposed frontogenesis.

For a more quantitative assessment, the vertical- and time-averaged salinity gradient of the fiftieth cycle is plotted in Fig. 8 (the heavy dashed line), which contrasts sharply its initial uniform gradient (the solid line) and to be compared with the analytical curve (dotted line in Fig. 5). Given the model geometry, the distance coordinates 30 and 60 km correspond roughly to the tic marks 0 and 1 in the analytical solution. We have not overlaid the two solutions, since to convert the analytical solution to dimensional units, one needs to diagnose the time-averaged salinity flux from the numerical solution, a non-trivial task. Nor is it necessary since such conversion involves only a constant scaling factor and hence does not change the placement of the peaks and troughs and their relative heights. One sees therefore a close agreement between the two curves, in support of the analytical model despite its extreme simplification.

With the model front anchored at the shelf break, the main remaining question about its relevance is whether it can account for the observed frontal sharpness. To address this question, we have plotted in X's the observed salinity gradient of a climatological front (Linder and Gawarkiewicz, 1998, based on the lower right panel of their Fig. 10). They have used depth-bin averaging to combine historical data to produce a climatological front on a nominal cross-shore transect, and the X's are the estimated slope of the tangent to their curve, with the peak aligned with that of the model front. It is seen that the observed values fall practically on the standard curve. Such close agreement is unexpected and must be somewhat fortuitous since there is no particular reason that the standard curve should be more representative than the other curves and there is large uncertainty in estimating the observed gradient. In any event, the comparison suggests that although the model front is not particularly sharp with its gradient limited to doubling that of the inshore water, such gradient contrast in fact is commensurate with that observed.

We have also conducted model runs with the forcing period halved and doubled, and the results are shown in Fig. 8 as dotted and thin dashed lines, respectively. The curves are similar if the forcing amplitude is halved and doubled, which are not shown. The progression of the curves is consistent with the analytical prediction (Section 2.4). As discussed therein, a longer period or a stronger wind would increase the diffusive depth and the local diffusivity at this depth, which is indeed reflected in the offshore migration and deepening of the trough. On the other hand, we have expected the frontal gradient to weaken as it is subjected to increasing eddy mixing, which would strongly constrains the offshore boundary of the front; both these features are clearly seen in the numerical curves. With the above comparison, the numerical calculations have essentially validated the analytical model.

While numerical solution agrees with the analytical solution as regards the vertical mean field, it contains vertical structure not addressed by the analytical model. For example, the analytical model has assumed for

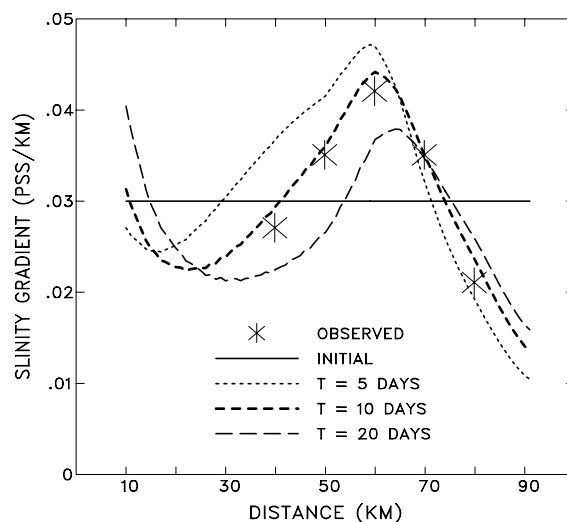


Fig. 8. Vertical- and time-averaged cross-shore salinity gradient from the unstratified runs with different forcing periods, as well as the initial uniform gradient. Plotted in X's are the observed gradient based on Linder and Gawarkiewicz (1998, lower right panel of their Fig. 10). They are the estimated slopes of the tangent to their curve, with the maximum aligned with the peak of the 10-day curve.

simplicity a mean field that is vertically uniform. With the horizontal diffusivity being a dynamical property, such limit may be approached if the cross-shore flux (hence the gradient) is sufficiently small, a condition not strongly met by the numerical solution. There are at least two factors that may contribute to vertical variation of the mean field. First, the no-normal flux at the bottom implies a tilt in the property line if the bottom is sloped, as seen in Fig. 7. Second, the horizontal diffusivity, as seen in Fig. 4c is highly heterogeneous in the vertical, being confined largely to the Ekman layer. In fact, as noted in Section 2.3, the reduction in the total diffusivity beyond the diffusive depth is due solely to the vanishing bottom Ekman flow, so the frontal gradient is enhanced near the bottom, a feature in fact discernible in Fig. 7b.

While unstratified solution has supported the proposed frontogenesis, and captured the essential features of the front, it is nonetheless of interest to see how the front may be modified when density stratification is allowed, as discussed next.

3.3. Stratified solution

To include the density stratification, we simply carried out calculations without suppressing the equation of state. The imposed boundary values of salinity and temperature yield a density of 25.2 and 26.2 σ_t at the inshore and offshore boundaries, respectively. The vertical viscosity and diffusivity in the model now resume their nominal parameterization based on turbulence closure. The time sequence of the solution (not shown) exhibits the following behavior. During the upwelling-favorable phase of the wind cycle, the fresh and cold (but less dense) inshore water moves seaward over the denser offshore water while the latter moves up the slope near the bottom, and the ensuing density stratification limits the vertical mixing to the surface and bottom layers. When the wind reverses, the surface water is advected shoreward and the bottom water seaward, which would gradually erode the pycnocline. Since the fluid may not be top-heavy without triggering overturning, isopycnals would never tilt shoreward. In other words, due to asymmetry in the vertical mixing, a mean pycnocline would develop even when forced by an oscillatory wind.

The mean salinity (averaged over the fiftieth cycle) is shown in Fig. 7c, which clearly exhibits the pycnocline just described. As in the unstratified solution, there is a front near the shelf break, but because of the density stratification, the isohalines are more strongly sloped, which represents a more realistic simulation of the observed situation. Such a density front would generate a cross-shore circulation with shoreward bottom flow and seaward surface flow, which reinforces the asymmetry between the positive and negative phase of the wind. Compared to the unstratified case, the surface front is displaced about 10 km farther offshore and its sharpness remains more or less the same, whereas the bottom front is pushed almost 20 km onshore and is significantly sharpened.

The stratified and unstratified solutions are further compared in Fig. 9, which shows the time evolution of surface and bottom salinity over two equilibrium cycles. At the surface, the frontal excursion is somewhat less in the stratified case because the surface velocity is weaker on average due to stronger surface layer mixing. Associated with the seaward frontal displacement in the stratified case, the salinity gradient on the shelf becomes much weaker as compared to that in the unstratified case. This is clearly due to enhanced mixing, similar to the unstratified case of longer forcing period, as discussed earlier. As expected, the movement of the bottom front is 180° out of phase with that of the surface front in both unstratified and stratified cases, but the frontal excursions are greater in the latter case because the front is anchoring at a shallower depth where the bottom flow is stronger. The sharper bottom front and its more inshore location in the stratified case is a result of the cross-frontal circulation. The along-shore geostrophic current associated with the front drives a convergent bottom flow at the foot of the front.

Despite the notable differences between the stratified and unstratified model runs, our model results seem to suggest that shear dispersion discussed in the analytical model remains the dominant frontogenesis mechanism even in the stratified case. In fact, without the wind forcing and the resulting shear flow, the model is unable to generate a shelf-break front from an initial density field of uniform gradient. The stratified model is one step closer to reality, but it is still highly idealized. For example, there should be surface evaporative cooling associated with the wind forcing. We neglected this in order to isolate the effects of wind and to facilitate a direct comparison with the analytical model. In a test run where evaporation is included, the enhanced vertical mix-

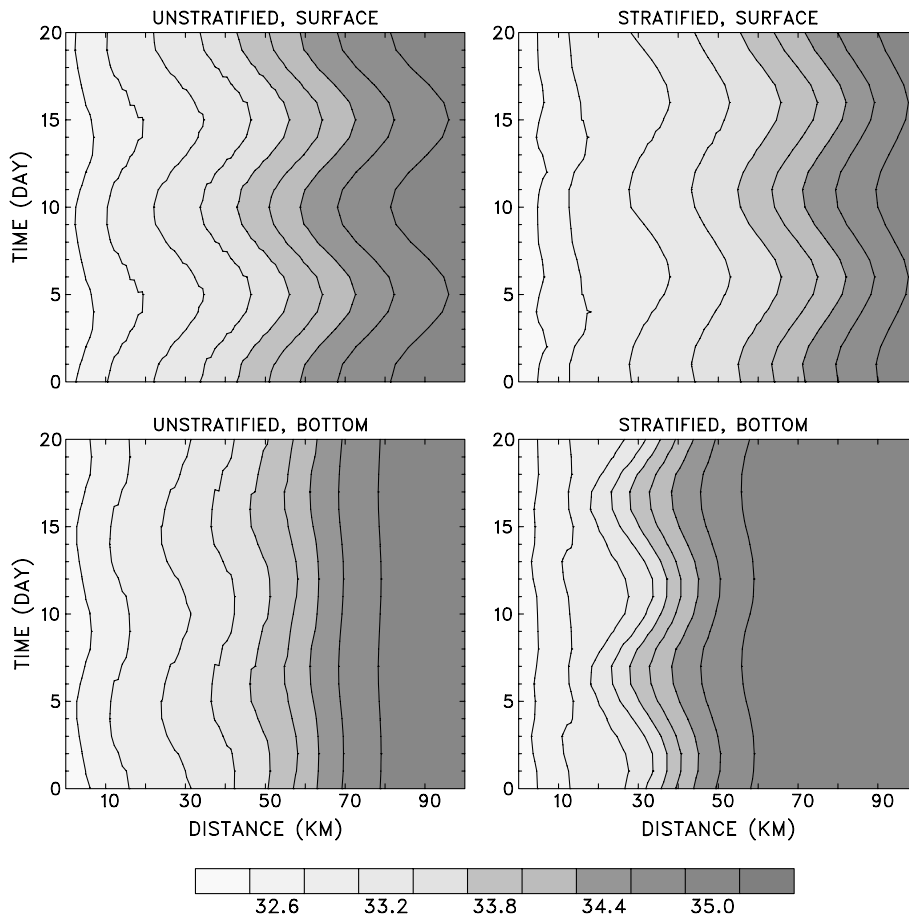


Fig. 9. Salinity variations at surface (upper row) and bottom (lower row) over two equilibrium cycles for unstratified (left column) and stratified (right column) cases.

ing pushes the bottom front farther offshore and anchors it more firmly at the shelf-break, in closer agreement with observations.

4. Discussion

Together with [Ou et al. \(2003\)](#), we have identified three regimes of horizontal mixing in the coastal ocean as one proceeds offshore: they are associated with tides, wind-driven motion and meso-scale eddies, progressively. The first two are through oscillatory shear dispersion explicitly modeled, the transition being due to their disparate forcing timescales; the last is merely conjectured as limited to the slope water. It is the minimum mixing between these regimes that gives rise to the tidal and shelf-break fronts. The mechanistic unification of these two prominent but seemingly unrelated fronts lends support to this overlooked category of frontogenesis that stems from spatial inhomogeneity in the horizontal mixing.

This two-dimensional cross-shore view of the shelf-break front differs from some recent studies that stress its along-shore evolution and gradual emergence. While these latter studies have delineated important dynamical features of the front, they fail to explain its anchoring at the shelf break – a defining character of the front, which is well established even at the upstream end of the Mid-Atlantic Bight. According to the present model, such topographic confinement merely reflects strong mixing from both sides: the wind-induced shear dispersion effective up to the outer shelf, and eddy mixing of the slope water.

In summer, there is little wind mixing to curb the inshore edge of the front, but paradoxically, the reduced mixing also enables the sub-thermocline front to persist through the summer months. In terms of the property

balance (2.25), this asymmetry stems from the importance of the secular term during frontolysis, so the property field deviates far from equilibrium attainable during frontogenesis on account of the large diffusivity and hence short diffusive timescale.

The main outcome of the analytical model is the derivation of the shear-induced diffusivity, which is a function of the motion field only. With such diffusivity known, one may then determine the property field whether or not it is subjected to surface fluxes. It is to isolate the effect of shear dispersion that we have neglected the surface fluxes, so the cross-shore flux is necessarily uniform in the steady state. In reality, only the salinity field satisfies such requirement; the thermal field, on the other hand, is subjected to surface cooling in winter, so there is offshore increase in the heat flux (directed shoreward), which would enhance the thermal front. In other words, the upper limit of gradient doubling at the front can be exceeded by non-conservative property fields. It should also be mentioned that such upper bound on the frontal gradient refers only to the mean field. For the instantaneous field, the frontal gradient could conceivably be greater, depending on the excursion distance during the forcing cycle. This is clearly seen in Fig. 9 when it is compared with Fig. 7.

From the numerical solution, we see that many complications would arise when the ocean is stratified, which could have significant implications on the frontogenesis. These include the density-driven cross-frontal circulation, the asymmetry in the vertical mixing within the forcing cycle, extreme heterogeneity in the vertical diffusivity due to stratification, and the surface cooling effect. Obviously addressing these stratified effects lies beyond the scope of the present study, which nonetheless points to a fertile ground for future study of frontogenesis.

Acknowledgements

As this paper contributes to the special volume commemorating Gabe Csanady's 80th birthday, it is fitting to acknowledge his tremendous impact on physical oceanography in general and frontal study in particular. Some his original ideas have so ingrained in our standard thinking that they are often not explicitly accredited, a testimonial to his far-reaching influence. Personally, H.W. Ou has been inspired by Gabe's course on coastal dynamics when he was a graduate student and has benefited greatly from their joint participation in the DOE-funded project "Shelf-Edge Exchange Processes" in the early eighties. The authors want to thank anonymous reviewers for comments that have led to significant improvement of the paper. This work is supported by the National Science Foundation through Grants OCE-00-02425 and OPP-01-25177.

Appendix. Analytical solution

The equation governing the perturbation concentration is (2.28)

$$C''_{zz} + m^2 C' = au', \quad (\text{A.1})$$

where $m^2 \equiv i2\pi$, $a \equiv 240\bar{C}_x$, and u' is the wind-driven motion given by (2.17). The boundary conditions to be satisfied are

$$C'_z = 0 \quad \text{at } z = 0, -h. \quad (\text{A.2})$$

The solution for the three slabs as defined in the wind-driven model can be easily obtained

$$C'_s = \frac{a}{m^2} u'_s + A \cosh(mz), \quad (\text{A.3})$$

$$C'_i = \frac{a}{m^2} u'_i + B \cosh(mz) + C \sinh(mz), \quad (\text{A.4})$$

$$C'_b = \frac{a}{m^2} u'_b + D \cosh[m(z+h)]. \quad (\text{A.5})$$

The integration constants can be determined by matching C' and C'_z at the boundaries of the slabs to yield

$$C = -\frac{a}{m^2} (u'_i - u'_s) \sinh(mh_E), \quad (\text{A.6})$$

$$B = \frac{1}{\sinh(mh)} \left[C \cosh(mh) + \frac{a}{m^2} (u'_b - u'_i) \sinh(mh_E) \right], \quad (\text{A.7})$$

$$A = B - C \frac{\cosh(mh_E)}{\sinh(mh_E)}, \quad (\text{A.8})$$

$$D = \frac{1}{\sinh(mh_E)} \{-B \sinh[m(h - h_E)] + C \cosh[m(h - h_E)]\}. \quad (\text{A.9})$$

The property flux is

$$F = \frac{1}{2} \text{re} \left\{ \int_{-h}^0 u^* C' dz \right\}, \quad (\text{A.10})$$

which is the sum of the fluxes in the three slabs given by

$$F_s = \frac{1}{2} \text{re} \left\{ \frac{1}{m} u_s^* A \sinh(mh_E) \right\}, \quad (\text{A.11})$$

$$F_i = \frac{1}{2} \text{re} \left\{ \frac{1}{m} u_i^* [B(-\sinh(mh_E) + \sinh(m[h - h_E])) + C(\cosh(mh_E) - \cosh(m[h - h_E]))] \right\}, \quad (\text{A.12})$$

$$F_b = \frac{1}{2} \text{re} \left\{ \frac{1}{m} u_b^* D \sinh(mh_E) \right\}. \quad (\text{A.13})$$

The total diffusivity can be calculated from (2.27). Since the mean gradient appears as multiplication factor on both sides of the equation, the total diffusivity is a function only of the motion field.

References

- Beardsley, R.C., Chapman, D.C., Brink, K.H., Ramp, S.R., Schlitz, R., 1985. The Nantucket Shoals Flux Experiment (NSFE79). Part I: Basic description of the current and temperature variability. *J. Phys. Oceanogr.* 15, 713–748.
- Chapman, D.C., 1986. A simple model of the formation and maintenance of the shelf/slope front in the Middle Atlantic Bight. *J. Phys. Oceanogr.* 16, 1273–1279.
- Chapman, D.C., Lentz, S.J., 1994. Trapping of a coastal density front by the bottom boundary layer. *J. Phys. Oceanogr.* 24, 1465–1479.
- Chapman, D.C., 2000. Boundary layer control of buoyant coastal currents and the establishment of a shelfbreak front. *J. Phys. Oceanogr.* 30, 2941–2955.
- Chen, D., Liu, T.W., Tang, W., Wang, Z., 2003a. Air–sea interaction at an oceanic front: implications for frontogenesis and primary production. *Geophys. Res. Lett.* 30, 1745. doi:10.1029/2003GL01753.
- Chen, D., Ou, H.W., Dong, C., 2003b. A model study of internal tides in coastal frontal zone. *J. Phys. Oceanogr.* 33, 170–187.
- Churchill, J.H., Levine, E.R., Connors, D.N., Cornillon, P.C., 1993. Mixing of shelf, slope and Gulf Stream water over the continental slope of the Middle Atlantic Bight. *Deep-Sea Res. I* 40, 1063–1085.
- Csanady, G.T., 1978. Wind effects on surface to bottom fronts. *J. Geophys. Res.* 83, 4633–4640.
- Csanady, G.T., 1982. *Circulation in the Coastal Ocean*. D. Reidel Publishing Company, Dordrecht, 279pp.
- Csanady, G.T., 1984. The influence of wind stress and river runoff on a shelf-sea front. *J. Phys. Oceanogr.* 14, 1383–1392.
- Fedorov, K.N., 1983. *The Physical Nature and Structure of Oceanic Fronts*. Lecture Notes on Coastal and Estuarine Studies. Springer-Verlag, New York, 333pp.
- Fisher, H.B., List, E.J., Koh, R.C.Y., Imberger, J., Brooks, N.H., 1979. *Mixing in Inland and Coastal Waters*. Academic Press, New York, 483pp.
- Flagg, C.N., Beardsley, R.C., 1978. On the stability of the shelf water/slope water front south of New England. *J. Geophys. Res.* 83 (C9), 4623–4632.
- Gawarkiewicz, G., Bahr, F., Beardsley, R.C., Brink, K.H., 2001. Interaction of a slope eddy with the shelfbreak front in the Middle Atlantic Bight. *J. Phys. Oceanogr.* 31, 2783–2796.
- Geyer, W.R., Signell, R.P., 1992. A reassessment of the role of tidal dispersion in estuaries and bays. *Estuaries* 15, 97–108.
- Hill, A.E., Simpson, J.H., 1989. On the interaction of thermal and haline fronts. The Islay front revisited. *Estuar. Coast. Shelf Sci.* 28, 495–505.
- Houghton, R.W., 1997. Lagrangian flow at the foot of a shelfbreak front using a dye tracer injected into the bottom boundary layer. *Geophys. Res. Lett.* 24, 2035–2038.
- Hsueh, Y., Cushman-Roisin, B., 1982. On the formation of surface to bottom fronts over steep topography. *J. Geophys. Res.* 88, 743–750.
- Linder, C.A., Gawarkiewicz, G., 1998. A Climatology of the shelfbreak front in the Middle-Atlantic Bight. *J. Geophys. Res.* 103, 18405–18423.
- Mellor, G.L., 1982. Development of a turbulence closure model for geophysical fluid problem. *Rev. Geophys. Space Phys.* 20, 851–875.
- Narayanan, C., Garvine, R.W., 2002. Formation of a shelfbreak front by freshwater discharge. *Dyn. Atm. Oceans* 36, 103–124.
- Okubo, A., 1967. The effect of shear in an oscillatory current on horizontal diffusion from an instantaneous source. *Int. J. Oceanol. Limnol.* 1, 194–204.

- Ou, H.W., 1983. Some two-layer models of the shelf-slope front: geostrophic adjustment and its maintenance. *J. Phys. Oceanogr.* 13, 1798–1808.
- Ou, H.W., Aikman III, F., Houghton, R.W., 1988. Complex empirical orthogonal function analysis of thermister chain data near a shelf-slope front. *Cont. Shelf Res.* 8, 711–728.
- Ou, H.W., Dong, C., Chen, D., 2003. Tidal diffusivity: a mechanism for frontogenesis. *J. Phys. Oceanogr.* 33, 840–847.
- Pickart, R.S., 2000. Bottom boundary layer structure and detachment in the shelfbreak jet of the Middle Atlantic Bight. *J. Phys. Oceanogr.* 30, 2668–2686.
- Smolarkiewicz, P.K., 1984. A fully multidimensional positive definite advection transport algorithm with small implicit diffusion. *J. Comp. Phys.* 54, 325–336.
- Ullman, D.S., Cornillon, P.C., 1999. Satellite-derived sea surface temperature fronts on the continental shelf off the northeast U.S. coast. *J. Geophys. Res.* 104 (C10), 23459–23478.
- Wang, D.-P., 1982. Development of a three-dimensional limited-area (island) shelf circulation model. *J. Phys. Oceanogr.* 12, 605–617.
- Wright, D.G., 1989. On the alongshore evolution of an idealized density front. *J. Phys. Oceanogr.* 19, 532–541.
- Zimmerman, J.T.F., 1986. The tidal whirlpool: a review of horizontal dispersion by tidal and residual currents. *Nether. J. Sea. Res.* 20, 133–154.